Predictive ZVS Control With Improved ZVS Time Margin and Limited Variable Frequency Range for a 99% Efficient, 130-W/in^3 MHz GaN Totem-Pole PFC Rectifier

Qingyun Huang, *Member, IEEE*, Ruiyang Yu, Qingxuan Ma*, Student Member, IEEE*,
and Alex Q. Huang, *Fellow, IEEE*

***Abstract*—This paper proposes a predictive zero-voltage-switching (ZVS) control with improved ZVS time margin and limited variable switching frequency range for a 99% efficient megahertz (MHz) GaN totem-pole power-factor-correction (PFC) rectifier. The conventional ZVS control methods for totem-pole PFC may lead to zero ZVS time margin and ultra-wide switching frequency range. This paper proposes that the synchronous rectifier (SR) turn-OFF current is a new degree of freedom for the ZVS control. Thus, the proposed cycle-by-cycle predictive ZVS control method controls the SR turn-OFF currents to extend the ZVS time margin and to reduce the maximum switching frequency. With the proposed ZVS control, the minimum ZVS time margin and a limited maximum switching frequency can be realized in a MHz GaN-based totem-pole PFC. With the improved ZVS time margin, the reliability for realizing ZVS is significantly improved. With the limited maximum frequency and the limited frequency range, the difficulty in high-speed current sensing and digital control is reduced, and the frequency-related loss is also reduced, which is important for improving the light-load efficiency. To accurately extract the current and timing parameters for the proposed ZVS control, an analytical model for the ZVS totem-pole PFC is proposed. The proposed ZVS control and analytical model are applicable over the full input and output voltage range, and over the full load range. In addition, a hybrid current control is proposed and implemented based on the proposed ZVS control. Finally, a 3.2-kW MHz GaN totem-pole PFC prototype is developed and tested with full-range ZVS, minimum ZVS time margin, limited switching frequency range, 99% peak efficiency, and 130-W/in^3 power density based on the proposed ZVS control and system control strategy. The realized efficiency, power level, and power density are among the best ever reported for the GaN-based totem-pole PFC.**

***Index Terms*—Gallium nitride (GaN), high density, high efficiency, high frequency, limited frequency range, totem-pole**

Manuscript received March 20, 2018; revised June 15, 2018 and August 15, 2018; accepted September 16, 2018. Date of publication October 21, 2018; date of current version May 2, 2019. This work was supported by Navitas Semiconductor. This paper was presented in part at the IEEE Applied Power Electronics Conference and Expo (APEC), Tampa, FL, USA, Mar. 26–30, 2017. Recommended for publication by Associate Editor Dr. X. Wu. *(Corresponding author: Qingyun Huang.)*

The authors are with the Department of Electrical and Computer Engineering, University of Texas at Austin, Austin, TX 78712 USA (e-mail:

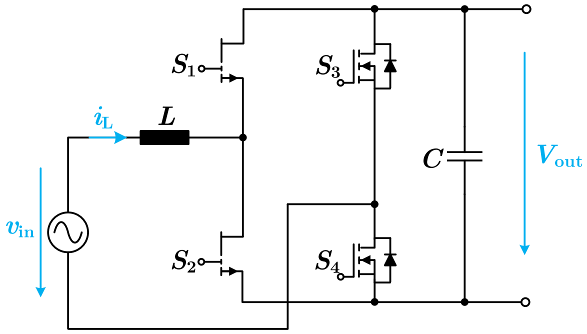

Fig. 1. Topology of Totem-pole PFC with GaN and Si MOSFETs.

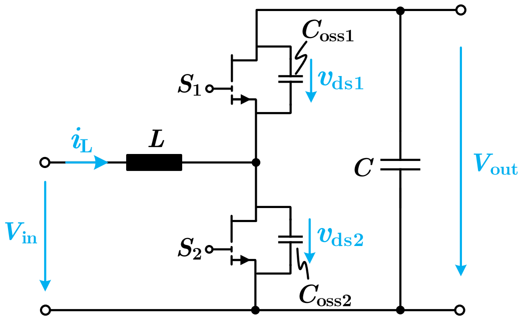

Fig. 2. Equivalent circuit during the positive half-line cycle.

PFC can work under hard switching condition. Besides, due to the ultra-high switching speed of the GaN devices, the switching losses are also significantly reduced compared with using Si MOSFETs [17]. The hard-switching GaN totem-pole PFC with 99% efficiency has been reported in [3] and [16]. However, the switching frequency must be relatively low to limit the switching loss, typically less than 120 kHz. Therefore, the power density of the hard-switching GaN totem-pole PFC rectifier is still similar to that of the conventional PFC rectifiers.

For the GaN devices, the turn-OFF loss is much less than the turn-ON loss [17]–[18]. So, to significantly increase the switching frequency, hence, the power density, the GaN-based zero-voltage-switching (ZVS) totem-pole PFC has been demonstrated [22]–[23] with high efficiency and high power density. Since the turn-ON loss is eliminated, the switching loss is still very low even if switching at megahertz (MHz) range. For MHz ZVS GaN totem-pole PFC, the size of the main inductor and the differential-mode (DM) filter are substantially reduced [21].

The MHz ZVS GaN totem-pole PFC has shown superior performance compared with the conventional PFC rectifiers. However, the ZVS control for the MHz GaN totem-pole PFC is still a very challenging technical issue, since it requires high-frequency cycle-by-cycle ZVS realization for the wide input voltage range, wide load range, and wide frequency range. One way to achieve ZVS is to operate the converter in the so-called critical mode (CRM) [24]–[26]. The equivalent circuit of the totem-pole PFC in the positive half-line cycle is shown in Fig. 2. Figs. 3(a) and 4(a) show the theoretical operation waveforms with the CRM control during the positive half-line cycle. As shown in Fig. 3(a), the SR MOSFET S_1 is immediately turned OFF after the inductor current i_L drops to zero. Then, the drain-to-source voltage V_{ds2} of the active switch S_2 is resonating to zero (resonance between the inductor and the C_{oss} of S_1 and S_2). The ZVS time margin is noted as T_{ZVS}. During T_{ZVS}, V_{ds2} is clamped to zero, and S_2 can be turned ON at any instant during T_{ZVS} for realizing ZVS of S_2. The corresponding state plane trajectory is depicted in Fig. 4(a). And the characteristic impedance Z_n is formulated as

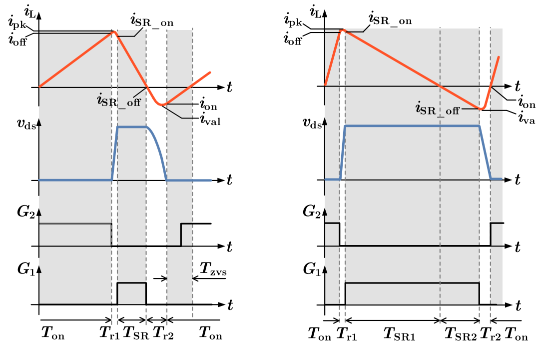

(a) (b)

Fig. 3. Theoretical waveforms with the state-of-the-art TCM ZVS control for totem-pole PFC. (a) CRM mode when $V_{in} \leq 0.5V_{out}$. (b) QSW mode when $V_{in} > 0.5V_{out}$.

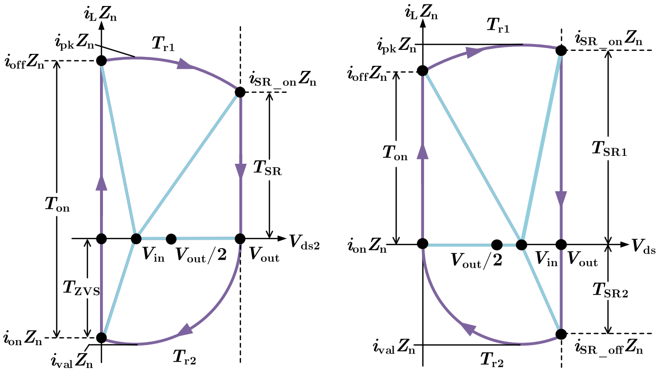

(a) (b)

Fig. 4. State plane trajectories with the state-of-the-art TCM ZVS control for totem-pole PFC. (a) CRM mode when $V_{in} \leq 0.5V_{out}$. (b) QSW mode when $V_{in} > 0.5V_{out}$.

$$Z_n = \sqrt{\frac{L}{2C_{oss}}} \tag{1}$$

where C_{oss} is the equivalent drain-to-source capacitance of S_1 and S_2, and L is the main inductor. However, the CRM control realizes ZVS only when the input voltage is lower than the half of the output voltage ($V_{in} \leq 0.5V_{out}$) [22], [29].

To achieve ZVS over the full input voltage range (from low line to high line, from zero volt to the peak voltage), the triangular current mode (TCM) ZVS control method is reported in [22], [23], and [27]–[30]. Fig. 3 shows the theoretical operation waveforms of the TCM ZVS control. Fig. 4 shows the corresponding state plane trajectories of the TCM ZVS control. When the input voltage is less than half of the output voltage ($V_{in} \leq 0.5V_{out}$), the TCM control makes the converter work at CRM as shown in Figs. 3(a) and 4(a). When the input voltage is higher than the half of the output voltage ($V_{\text{in}} > 0.5V_{\text{out}}$), the TCM control makes the converter work at quasi-square-wave (QSW) mode with an extended SR conduction time [22], [23], [27]–[30]. The extended SR conduction time allows the SR to be turned OFF with a negative current $i_{\text{SR\_off}}$ to aid the active switch achieving the ZVS. As shown in Fig. 3(b), when $V_{\text{in}} > 0.5V_{\text{out}}$ during the positive half-line cycle, the SR MOSEFT S_1 is not immediately turned OFF after the inductor current i_L drops to zero. On the contrary, S_1 conducts with the extended SR on-time T_{SR2} to make the inductor current continually drop to $i_{\text{SR\_off}}$, which is the required negative current to achieve the ZVS. Then, after S_1 is turned OFF, the drain-to-source voltage V_{ds2} of S_2 will be resonant to zero. The corresponding state plane trajectory is depicted in Fig. 4(b).

As shown in Figs. 3(b) and 4(b), this previously described TCM control does not provide any ZVS time margin ($T_{\text{ZVS}} = 0$) when $V_{\text{in}} > 0.5V_{\text{out}}$ [22], [23], [27]–[30]. With this state-of-the-art TCM ZVS control, the negative current is only sufficient to realize the ZVS for one instant when $V_{\text{in}} > 0.5V_{\text{out}}$. Thus, the active switch S_2 could still lose ZVS, even if S_2 is turned ON slightly before or after that instant. It is difficult to guarantee ZVS for every switching cycle with this state-of-the-art TCM ZVS control. The turn-ON loss may not be totally eliminated, and the efficiency is impacted if the switching frequency is high.

In addition to the issue of zero ZVS time margin, the state-of-the-art TCM ZVS control also does not provide any limit on the switching frequency. The variable switching frequency can become several MHz under light-load conditions, if the maximum switching frequency under full load is around 1 MHz. This ultra-high frequency severely impacts the light-load efficiency due to the high turn-OFF loss, magnetic core loss and high-frequency ac winding loss. Besides, it is also very challenging for the implementation of the high speed current sensor and the digital controller due to the high frequency and the wide frequency range. The valley skipping technique can limit the switching frequency [31], [32]. However, the valley skipping technique requires additional valley detection. And the valley skipping technique cannot continuously control the switching frequency. The discontinuous frequency distribution causes additional control issue. Besides, the valley skipping technique introduces the additional conduction loss due to the high-frequency ringing.

To solve these issues in the conventional TCM ZVS control, this paper proposes a predictive ZVS control method for the MHz GaN totem-pole PFC. The proposed predictive ZVS control can maintain the minimum ZVS time margin and limit the maximum switching frequency over the full range of input and output voltages and full range of the output power. This paper proposes that the SR turn-OFF current $i_{\text{SR\_off}}$ is a new degree of freedom for the ZVS control. And when the SR turn-OFF current is lower (more negative), the larger ZVS time margin and the lower switching frequency can be achieved. Moreover, the ZVS time margin and the switching frequency can be accurately and continuously controlled by controlling the SR turn-OFF current. Therefore, the proposed ZVS control method predictively controls the SR turn-OFF current to satisfy the ZVS requirement, the minimum ZVS margin requirement, and the maximum frequency limitation requirement. And, in this proposed ZVS control method, the SR turn-OFF current is predictively controlled by the extended SR conduction time T_{SR2}. To accurately extract the current and timing parameters for the proposed ZVS control, a detailed analytical model for the ZVS totem-pole PFC is also developed. The proposed predictive ZVS control and analytical model are applicable for the full range of the input voltage (from low line to high line) and the full range of the output power (from full load to light load). In addition, based on the proposed predictive ZVS control, this paper proposes a hybrid current control for the totem-pole PFC. The active switch turn-OFF instant is determined by the peak current comparison. The SR turn-OFF instant is determined by the required extended SR conduction time, which achieves the required SR turn-OFF current. This hybrid current control combines the benefits of the current mode control and the time-based control. Preliminary work on the proposed ZVS control and system control for the GaN totem-pole PFC was presented in [15]. This paper improves upon the work of [15] to include the detailed implementation of the developed 3.2-kW GaN totem-pole PFC prototype that achieves 99% efficiency and 130-W/in^3 power density, the enhanced experimental verification, and more details about the proposed control algorithm and the system control diagrams.

This paper is organized as follows. In Section II, the detailed descriptions of the proposed predictive ZVS control and the proposed system control strategy with the hybrid current control are included. Section III discusses the proposed analytical model for the ZVS totem-pole PFC. Section IV includes the calculations of the required SR turn-OFF current and the required extended SR conduction time based on the proposed ZVS control. Section V shows the improved ZVS time margin and limited switching frequency with the proposed ZVS control. In Section VI, a 3.2-kW-MHz ZVS GaN totem-pole PFC prototype with 99% efficiency, 130-W/in^3 power density is developed and tested to verify the proposed predictive ZVS control and current control strategy. Finally, Section VII concludes this paper.

II. PROPOSED PREDICTIVE ZVS CONTROL AND SYSTEM CONTROL STRATEGY

A. Description of the Proposed Predictive ZVS Control

The basic operation principles of the proposed predictive ZVS control is illustrated by the theoretical operation waveforms and the state plane trajectory as shown in Fig. 5. All the discussions are still based on the positive half-line cycle ($V_{\text{in}} > 0$) equivalent circuit as shown in Fig. 2. The analysis and discussions for the negative half-line cycle are similar. The only difference is that the roles of the S_1 and S_2 are interchanged.

As shown in Fig. 5, during the resonant time T_{r1}, S_1, and S_2 are both turned OFF. The S_2 drain-to-source voltage V_{ds2} is charged from zero to V_{out}. The inductor current i_{L} is resonant from the active switch turn-OFF current i_{off} to the SR turn-ON current $i_{\text{SR\_on}}$. The inductor peak current is i_{pk}. During the SR conduction time T_{SR1}, S_1 is turned ON, and S_2 is turned OFF. The inductor current i_{L} decreases linearly from $i_{\text{SR\_on}}$ to zero. During the extended SR conduction time T_{SR2}, S_1 is still ON,and S_2 is still OFF. The inductor current i_{L} decreases linearly from

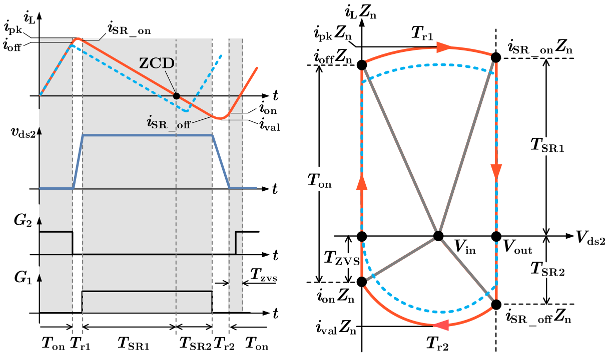

(a) (b)

Fig. 5. (a) Operation waveforms based on the proposed predictive ZVS control. (b) State plane trajectory based on the proposed predictive ZVS control.

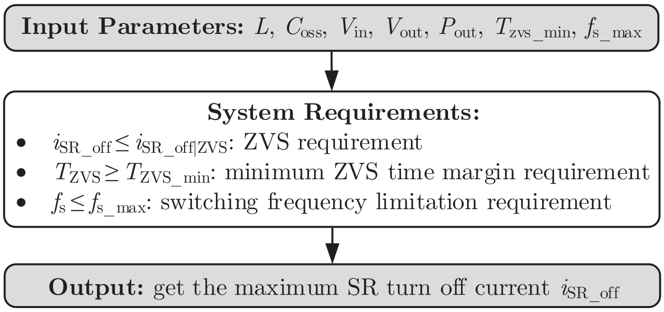

Fig. 6. Optimization procedure for calculating the required SR turn-OFF current based on the proposed ZVS control method.

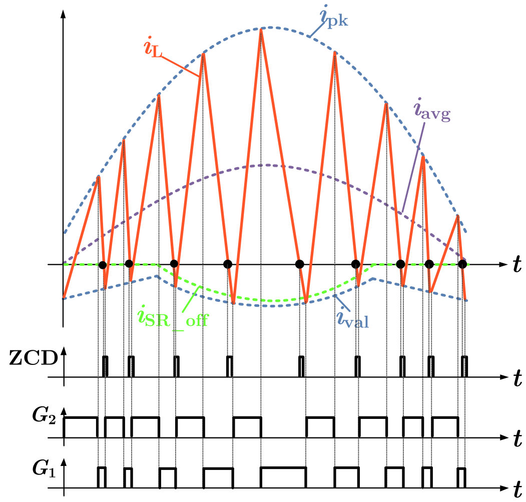

Fig. 7. Theoretical waveforms in the positive half line cycle based on the proposed ZVS control and system control strategy.

$i_{\mathrm{SR\_on}}$ to the SR turn-OFF current $i_{\mathrm{SR\_off}}$. During the resonant time T_{r2}, S_1 and S_2 are both turned OFF. V_{ds2} is discharged from V_{out} to zero. The inductor current i_{L} is resonant from the SR turn-OFF current $i_{\mathrm{SR\_off}}$ to the active switch S_2 turn-ON current i_{on}. The inductor valley current is i_{val}. During the active switch conduction time T_{on}, the inductor current i_L increases linearly from i_{on} to i_{off}. At the beginning of T_{on}, the equivalent "body diode," which is the third quadrant conduction of S_2 is conducting first. Then, S_2 can be turned ON at any instant during the ZVS time margin T_{ZVS}.

For the conventional TCM ZVS control [22], [23], [27]–[30], the SR turn-OFF current $i_{\mathrm{SR\_off}}$ (a negative current) is only required to be the maximum current $i_{\mathrm{SR\_off}\,|\,\mathrm{ZVS}}$ to achieve ZVS, which is calculated as

$$i_{\mathrm{SR\_off}}\,|_{\mathrm{ZVS}} = -\sqrt{\max\left\{\frac{V_o(2V_{\mathrm{in}}-V_{\mathrm{out}})}{Z_n^2},0\right\}}. \tag{2}$$

However, the state plane trajectory depicted in Fig. 5(b) shows that if $i_{\mathrm{SR\_off}}$ is lower (more negative), the initial energy stored in the inductor is larger for charging the C_{oss} of S_1 and for discharging the C_{oss} of S_2. Therefore, the ZVS time margin T_{ZVS} is larger. In addition, the operation waveforms in Fig. 5(a) show that if $i_{\mathrm{SR\_off}}$ is lower (more negative), the inductor valley current is lower and the inductor peak current is higher. Thus, the switching period is longer, and the switching frequency is lower. In addition, the ZVS time margin and the switching frequency can be accurately and continuously controlled by controlling the SR turn-OFF current (this will be illustrated in the next sections). Thus, the SR turn-OFF current is a new degree of freedom for the ZVS control. Therefore, in this paper, the proposed predictive ZVS control method predictively controls the SR turn-OFF current $i_{\mathrm{SR\_off}}$ (a negative current) to be the maximum value while achieving the ZVS, the minimum ZVS time margin and the maximum switching frequency limitation for the full range of the input voltage and the full range of the output power. The optimization procedure for calculating the required SR turn-OFF current based on the proposed ZVS control method is illustrated in Fig. 6. $T_{\mathrm{ZVS\_min}}$ is the required minimum ZVS time margin, and $f_{\mathrm{s\_max}}$ is the allowed maximum switching frequency.

As shown in Fig. 6, for the ZVS requirement, the SR turn-OFF current $i_{\mathrm{SR\_off}}$ should not be higher than $i_{\mathrm{SR\_off}\,|\,\mathrm{ZVS}}$ as

$$i_{\mathrm{SR\_off}} \le i_{\mathrm{SR\_off}}\,|_{\mathrm{ZVS}}\,. \tag{3}$$

For the minimum ZVS time margin requirement, the ZVS time margin T_{ZVS} should not be less than $T_{\mathrm{ZVS\_min}}$ as

$$T_{\mathrm{ZVS}} \ge T_{\mathrm{ZVS\_min}}. \tag{4}$$

For the switching frequency limitation requirement, the switching frequency f_s should not be higher than f_{s_max} as

$$f_s \le f_{s\_\mathrm{max}}. \tag{5}$$

Then, with the proposed ZVS control method, the SR turn-OFF current $i_{\mathrm{SR\_off}}$ is predictively controlled by the extended SR conduction time T_{SR2}, which is also calculated based on the system parameters and the sensed signals. The detailed mathematical model and the implementation of the controller will be illustrated in the next sections.

B. System Control Strategy With Hybrid Current Control

The theoretical waveforms in the positive half line cycle are shown in Fig. 7. Based on the proposed predictive ZVS control, a system control strategy is proposed in this paper. In this proposed

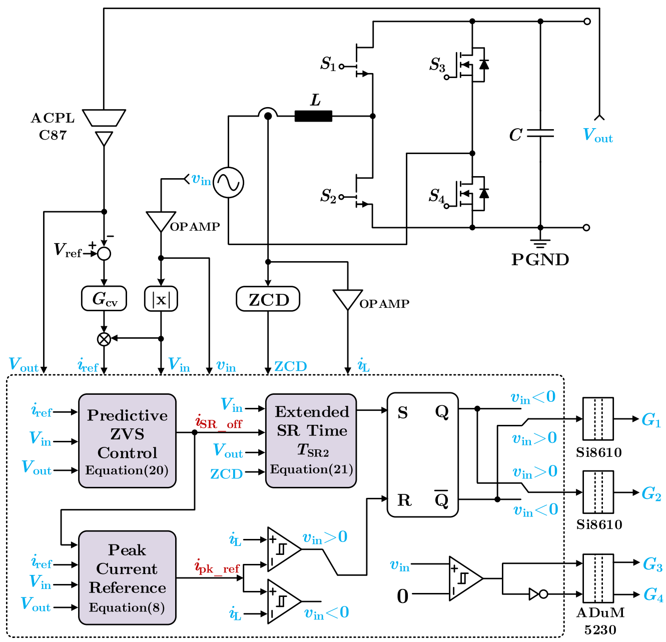

Fig. 8. Simplified control diagram of the proposed system control strategy.

control strategy, the turn-OFF instant of the SR is determined by the zero-crossing-detection (ZCD) signal and the required extended SR conduction time $T_{\rm SR2}$. The turn-OFF instant of the active switch is determined by the instantaneous peak current comparison. This control strategy combines the current mode control and the time-based current control.

The simplified control diagram is shown in Fig. 8. $i_{\rm ref}$ is the absolute value of the ac current reference. $V_{\rm in}$ is the absolute value of the ac voltage $v_{\rm in}$. Then, $i_{\rm ref}$ is the product of the voltage loop controller output and $V_{\rm in}$. The ZCD signal is generated by sensing the inductor current $i_{\rm L}$. With input signals ($i_{\rm ref}$, $V_{\rm in}$, and $V_{\rm out}$) and the system parameters (L, $C_{\rm oss}$, $T_{\rm ZVS\_min}$, and $f_{s\_\max}$), the proposed predictive ZVS control generates the required SR turn-OFF current $i_{\rm SR\_off}$ as presented in Fig. 6. Then, the extended SR conduction time $T_{\rm SR2}$ is calculated based on the aforementioned input signals and system parameters to achieve the required SR turn-OFF current $i_{\rm SR\_off}$. Therefore, after the controller obtains the ZCD signal, the SR is conducting for the extended SR conduction time $T_{\rm SR2}$. After $T_{\rm SR2}$, the SR is turned OFF and the active switch is turned ON. Thus, the turn-OFF instant of the SR is determined by the time-based current control.

The peak current reference $i_{\rm pk\_ref}$ is also calculated based on the input signals ($i_{\rm SR\_off}$, $i_{\rm ref}$, $V_{\rm in}$, and $V_{\rm out}$) and the system parameters (L and $C_{\rm oss}$). Then, the sensed inductor current i_L is compared with the peak current reference $i_{\rm pk\_ref}$ to generate the active switch turn-OFF signal. Thus, the turn-OFF instant of the active switch is determined by the current mode control.

In this hybrid control strategy, the timer is synchronized to the ZCD signal cycle by cycle. Thus, all the ON/OFF time of the SR and the active switch can be limited by the timer. This is the benefit of the time-based current control. Moreover, the peak current comparison can limit the peak current cycle by cycle, and this is the benefit of the current mode control. Therefore, the proposed control strategy combines the strengths of the current mode control and the time-based control.

In addition, for the totem-pole PFC, in the positive half-line cycle, S_1 is the SR, and S_2 is the active switch; in the negative half-line cycle, S_1 is the active switch and S_2 is the SR. Thus, the polarity of the analog comparator is changed according to the polarity of the input voltage $v_{\rm in}$ as shown in Fig. 8. The gating signals for S_1 and S_2 are also synthesized by the polarity of $v_{\rm in}$. Moreover, the gating signals for line-frequency switches S_3 and S_4 are directly determined by the polarity of $v_{\rm in}$.

III. ANALYTICAL MODEL FOR ZVS TOTEM-POLE PFC

The previous section describes the basic operation principles of the proposed predictive ZVS control. Based on the previous discussion, it is known that, the SR turn-OFF current $i_{\rm SR\_off}$ is another degree of freedom for the ZVS control. This section presents an analytical model for the proposed ZVS control. And all the discussion is based on the positive half-line cycle. And all the following calculations can be obtained based on Fig. 5(a) and (b).

In this analytical model, the SR turn-OFF current $i_{\rm SR\_off}$ is an input parameter. Thus, based on the analysis of the resonance during $T_{\rm r2}$ as shown in Fig. 5(b), the inductor valley current $i_{\rm val}$ is expressed as

$$i_{\rm val} = -\sqrt{\left(\frac{V_{\rm out}-V_{\rm in}}{Z_n}\right)^2 + i_{\rm SR\_off}^2}. \tag{6}$$

With this valley current, the turn-ON current $i_{\rm on}$ of the active switch is formulated as

$$i_{\rm on} = -\sqrt{i_{\rm val}^2 - \left(\frac{V_{\rm in}}{Z_n}\right)^2}. \tag{7}$$

The required inductor peak current $i_{\rm pk}$, which is determined by the valley current $i_{\rm val}$ and the required inductor average current $i_{\rm avg}$, is formulated as

$$i_{\rm pk} = 2i_{\rm avg} - i_{\rm val}. \tag{8}$$

And, the required average current $i_{\rm avg}$ is calculated as

$$i_{\rm avg} = i_{\rm ref} = \frac{\sqrt{2}P_{\rm out}}{V_{\rm in\_rms}^2}\sin(2\pi f_L t) \tag{9}$$

where $P_{\rm out}$ is the output power, $V_{\rm in\_rms}$ is the RMS value of the input voltage, $i_{\rm ref}$ is the reference of the inductor average current, and f_L is the ac line frequency. Then, based on the waveforms during $T_{\rm on}$ and $T_{\rm r1}$ as shown in Fig. 5(a) and (b), the active switch turn-OFF current $i_{\rm off}$ and the SR turn-ON current $i_{\rm SR\_on}$ are formulated as

$$i_{\rm off} = \sqrt{i_{\rm pk}^2 - \left(\frac{V_{\rm in}}{Z_n}\right)^2} \tag{10}$$

$$i_{\rm SR\_on} = \sqrt{i_{\rm pk}^2 - \left(\frac{V_{\rm out}-V_{\rm in}}{Z_n}\right)^2}. \tag{11}$$

Therefore, if the SR turn-OFF current $i_{\rm SR\_off}$ is given, all the other current values can be calculated based on (6)∼(11).

IV. REQUIRED SR TURN-OFF CURRENT AND EXTENDED SR CONDUCTION TIME

With the proposed ZVS control, the required SR turn-OFF current $i_{\text{SR\_off}}$ is determined by the ZVS requirement, the minimum ZVS time margin requirement, and the maximum frequency limitation requirement. All the calculations to find the required SR turn-OFF current $i_{\text{SR\_off}}$ are based on the proposed optimization procedure as shown in Fig 6. Again, all the analysis in this section is based on the positive half-line cycle. For the ZVS requirement, the required SR turn-OFF current $i_{\text{SR\_off}\,|\,\text{ZVS}}$ is calculated in (2). Thus, the SR turn-OFF current $i_{\text{SR\_off}}$ cannot be higher than $i_{\text{SR\_off}\,|\,\text{ZVS}}$. For the other two requirements, the required SR turn-OFF currents are analyzed as follows.

A. Minimum ZVS Time Margin Requirement

As shown in Fig. 5, during the ZVS time margin T_{ZVS}, the inductor current linearly increases from i_{on} to zero. Therefore, T_{ZVS} is calculated as

$$T_{\text{ZVS}} = -L\frac{i_{\text{on}}}{V_{\text{in}}}. \tag{12}$$

According to (6) and (7), i_{on} is expressed as

$$i_{\text{on}} = -\sqrt{\frac{V_{\text{out}}(V_{\text{out}} - 2V_{\text{in}})}{Z_n^2} + i_{\text{SR\_off}}^2}. \tag{13}$$

Thus, the ZVS time margin T_{ZVS} can be expressed as

$$T_{\text{ZVS}} = \frac{L}{V_{\text{in}}}\sqrt{\frac{V_{\text{out}}(V_{\text{out}} - 2V_{\text{in}})}{Z_n^2} + i_{\text{SR\_off}}^2}. \tag{14}$$

As shown in the aforementioned equation, the ZVS time margin can be continuously controlled by the SR turn-OFF current $i_{\text{SR\_off}}$. And if $i_{\text{SR\_off}}$ is lower (more negative in magnitude), the ZVS time margin T_{ZVS} is larger. According to the ZVS time margin requirement, the ZVS time margin T_{ZVS} should not be lower than the required minimum ZVS time margin $T_{\text{ZVS\_min}}$, as discussed in (4). Based on (4) and (12)∼(14), the SR turn-OFF current $i_{\text{SR\_off}}$ should satisfy the following inequation for the minimum ZVS time margin requirement. The ZVS time margin related item k_1 is also denoted as follows:

$$i_{\text{SR\_off}}^2 \geq k_1 = \frac{V_o(2V_{\text{in}} - V_{\text{out}})}{Z_n^2} + \left(\frac{T_{\text{ZVS\_min}}V_{\text{in}}}{L}\right)^2. \tag{15}$$

However, the lower the SR turn-OFF current $i_{\text{SR\_off}}$ is (more negative in magnitude), the larger the circulating energy is. Thus, $i_{\text{SR\_off}}|_{T_{\text{ZVS}} \geq T_{\text{ZVS\_min}}}$, which should be the maximum SR turn-OFF current (a negative current) satisfying the minimum ZVS time margin requirement, can be calculated as

$$i_{\text{SR\_off}}\,|_{T_{\text{ZVS}} \geq T_{\text{ZVS\_min}}} = -\sqrt{\max\{k_1,\quad 0\}}. \tag{16}$$

According to (15) and (16), this minimum ZVS time margin requirement is only dependent on V_{in} and V_{out}, if the circuit parameters are fixed.

B. Maximum Switching Frequency Limitation Requirement

To simplify the calculation of the switching period T_s, the inductor current can be modeled as linearly increasing from i_{val} to i_{pk}, and then, linearly decreasing from i_{pk} to i_{val} [29]. Thus, the switching period T_s and the switching frequency f_s can be expressed as

$$T_s = \frac{1}{f_s} = L\frac{i_{\text{pk}} - i_{\text{val}}}{V_{\text{in}}} + L\frac{i_{\text{pk}} - i_{\text{val}}}{V_{\text{out}} - V_{\text{in}}} \tag{17}$$

where i_{pk} and i_{val} can be expressed by the SR turn-OFF current by $i_{\text{SR\_off}}$ based on (6)∼(9). As shown in Fig. 5(a), if $i_{\text{SR\_off}}$ is lower (more negative), the switching frequency f_s is lower. According to the maximum switching frequency limitation requirement, the switching frequency f_s should not be higher than the required maximum switching frequency $f_{s\text{\_max}}$, as presented in (5). Based on (5) and (17), the SR turn-OFF current $i_{\text{SR\_off}}$ should satisfy the following inequation for the maximum switching frequency limitation requirement. The switching frequency related item k_2 is also denoted as follows:

$$\begin{aligned} i_{\text{SR\_off}}^2 \geq k_2 = {}& \left[\max\left\{\frac{V_{\text{in}}(V_{\text{out}} - V_{\text{in}})}{2Lf_{\text{sw\_max}}V_{\text{out}}} - i_{\text{avg}}, 0\right\}\right]^2 \\ & - \left(\frac{V_{\text{out}} - V_{\text{in}}}{Z_n}\right)^2. \end{aligned} \tag{18}$$

Again, the lower the SR turn-OFF current $i_{\text{SR\_off}}$ is (more negative in magnitude), the larger the circulating energy is. Thus, $i_{\text{SR\_off}}|_{f_{\text{sw}} \leq f_{\text{sw\_max}}}$, which should be the maximum SR turn-OFF current (a negative current) satisfying the maximum switching frequency limitation requirement, can be calculated as

$$i_{\text{SR\_off}}\,|_{f_{\text{sw}} \leq f_{\text{sw\_max}}} = -\sqrt{\max\{k_2,\quad 0\}}. \tag{19}$$

According to (18) and (19), this maximum switching frequency limitation requirement is not only dependent on V_{in} and V_{out} but also dependent on the output power P_{out}, which is related to the average inductor current i_{avg}.

C. Required SR Turn-off Current

Combining all the aforementioned requirements, the SR turn-OFF current (a negative current) should be controlled as the maximum value that satisfies all the ZVS requirement, the minimum ZVS time margin requirement and the maximum switching frequency limitation requirement. The required SR turn-OFF current $i_{\text{SR\_off}}$ is formulated as

$$i_{\text{SR\_off}} = -\sqrt{\max\{0,\quad k_1,\quad k_2\}}. \tag{20}$$

This equation means that the required SR turn-OFF current $i_{\text{SR\_off}}$ is determined by the maximum value among k_1, k_2, and zero. And, k_1 and k_2 have been expressed in (15) and (18), respectively. The values calculated in (20) are the solutions of the proposed optimization procedure for calculating the required SR turn-OFF current based on the proposed ZVS control method.

Fig. 9 shows the required SR turn-OFF currents $i_{\text{SR\_off}}$ under different load conditions. The parameters for Fig. 9 are listed as follows: $V_{\text{in}} = 240$ VAC, $V_{\text{out}} = 400$ V, $P_{\text{out}} = 1.6$ kW, $L = 9.5\,\mu$H, $C_{\text{oss}} = 120$ pF, $T_{\text{ZVS\_min}} = 30$ ns, and $f_{s\text{\_max}} = 1.5$ MHz.

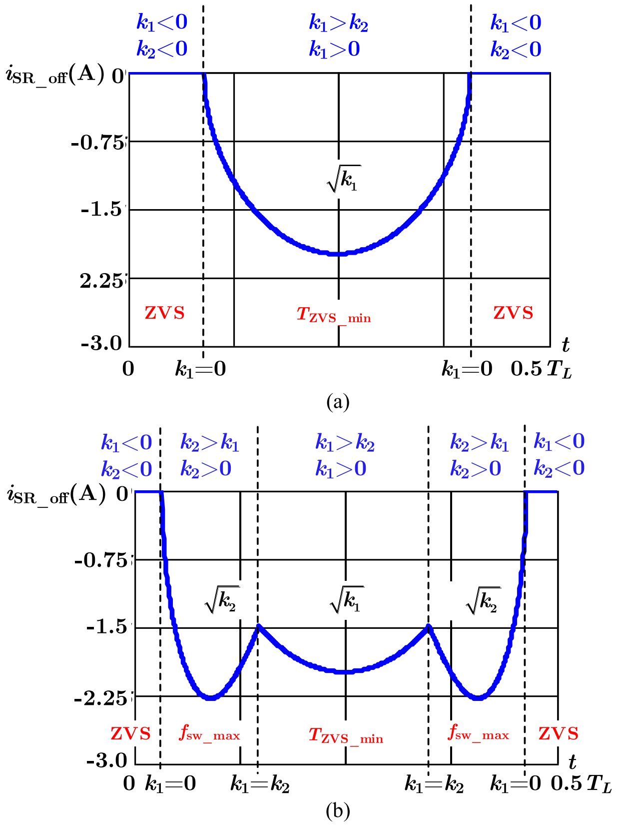

Fig. 9. (a) Required SR turn-OFF current under the full-load condition. (b) Required SR turn-OFF current under 20% of the full load condition.

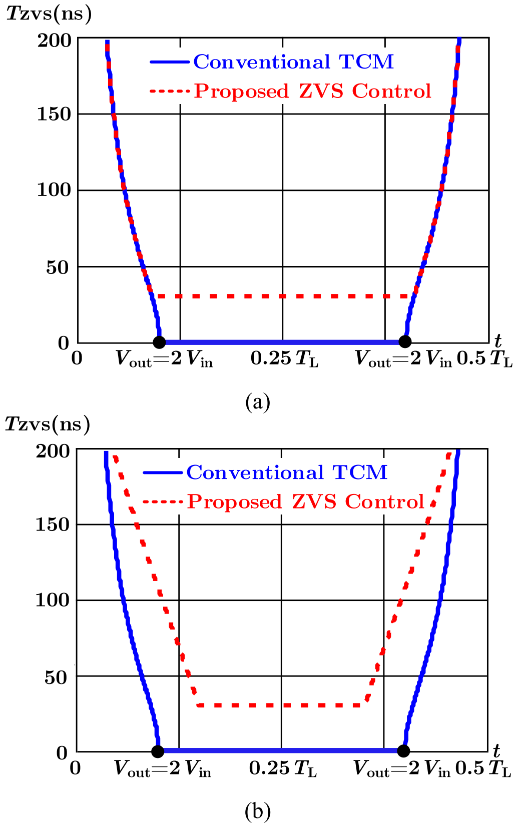

Fig. 10. (a) ZVS time margin distribution under the full-load condition. (b) ZVS time margin distribution under 20% of the full-load condition.

Under the heavy load condition, the required SR turn-OFF current $i_{\mathrm{SR\_off}}$ is shown in Fig. 9(a). In Fig. 9(a), when $k_1 > k_2$ and $k_1 > 0$, the required SR turn-OFF current $i_{\mathrm{SR\_off}}$ is determined by the minimum ZVS time margin requirement; when $k_1 < 0$ and $k_2 < 0$, $i_{\mathrm{SR\_off}}$ is determined by the ZVS requirement. Under the heavy load condition, since the original maximum switching frequency under heavy load condition is less than the maximum switching frequency limitation f_{s_max}, the required SR turn-off current $i_{\mathrm{SR\_off}}$ is dominated by the ZVS requirement and the minimum ZVS time margin requirement. At 20% load, the required SR turn-OFF current $i_{\mathrm{SR\_off}}$ is shown in Fig. 9(b). In Fig. 9(b), when $k_1 > k_2$ and $k_1 > 0$, the required SR turn-OFF current $i_{\mathrm{SR\_off}}$ is determined by the minimum ZVS time margin requirement; when $k_2 > k_1$ and $k_2 > 0$, $i_{\mathrm{SR\_off}}$ is determined by the maximum frequency limitation requirement; and when $k_1 < 0$ and $k_2 < 0$, $i_{\mathrm{SR\_off}}$ is determined by the ZVS requirement.

D. Extended SR Conduction Time

As discussed previously, the proposed hybrid current control combines the current mode control and the time-based control. The active switch turn-OFF instant is determined by the peak current comparison. And the SR turn-OFF instant is determined by the ZCD signal and the required extended SR conduction time T_{SR2}. During the extended SR conduction time T_{SR2}, the inductor current is linearly decreasing. And the SR turn-OFF current $i_{\mathrm{SR\_off}}$ is linearly controlled by T_{SR2}. Therefore, by controlling the extended SR conduction time T_{SR2}, the SR turn-OFF current $i_{\mathrm{SR\_off}}$ can be predictively controlled as the required value defined in (20) to satisfy all the aforementioned requirements, including the ZVS requirement, the minimum ZVS time margin requirement, and the maximum frequency limitation requirement. Therefore, the extended SR conduction time T_{SR2} is calculated as

$$T_{\mathrm{SR2}} = -L\frac{i_{\mathrm{SR\_off}}}{V_{\mathrm{out}} - V_{\mathrm{in}}} \tag{21}$$

where the required SR turn-OFF current $i_{\mathrm{SR\_off}}$ is obtained in (20).

V. IMPROVED ZVS TIME MARGIN AND LIMITED SWITCHING FREQUENCY

With the proposed ZVS control, the ZVS time margin can be improved, and the switching frequency can be limited based on the system requirements. Figs. 10 and 11 show the improved ZVS time margin and the limited switching frequency respectively. The parameters for Figs. 10 and 11 are the same with those for Fig. 9, which are listed again as follows: $V_{\mathrm{in}} = 240$ VAC, $V_{\mathrm{out}} = 400$ V, $P_{\mathrm{out}} = 1.6$ kW, $L = 9.5$ μH, $C_{\mathrm{oss}} = 120$ pF, $T_{\mathrm{ZVS\_min}} = 30$ ns, and $f_{s\_\mathrm{max}} = 1.5$ MHz.

Fig. 10(a) shows the ZVS time margin distributions under the full load condition with the conventional TCM ZVS control and the proposed ZVS control. As shown in Fig. 10(a), with the

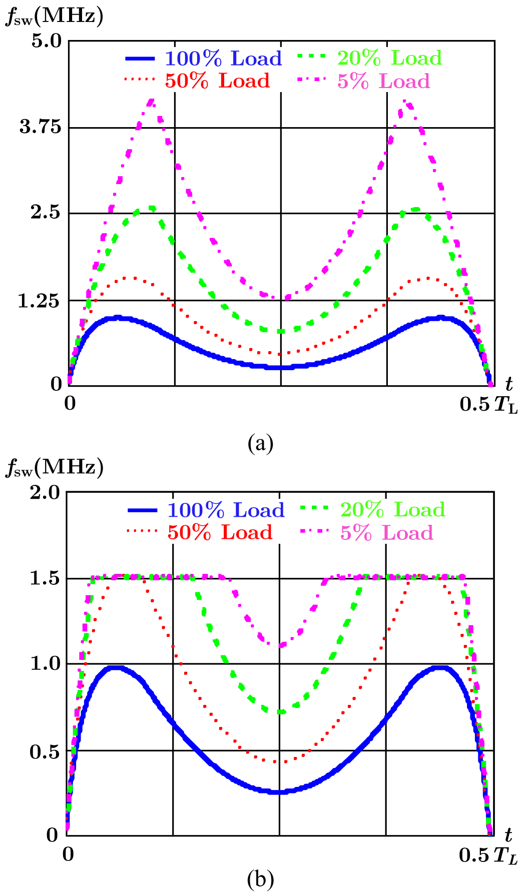

(a)

(b)

Fig. 11. (a) Switching frequency distribution with the conventional TCM control. (b) Switching frequency distribution with the proposed ZVS control.

conventional TCM ZVS control, the ZVS time margin is zero when $V_{in} > 0.5V_{out}$. However, with the proposed ZVS control, the ZVS time margin can be kept no less than 30 ns, which is the required minimum ZVS time margin. Fig. 10(b) shows the ZVS time margin distribution under 20% of the full load condition. As shown in Fig. 10(b), the ZVS time margin is increased when the maximum switching frequency limitation dominates the required SR turn-OFF current.

Fig. 11(a) shows the switching frequency distribution with the conventional TCM ZVS control from the full load to 5% of the full load. As shown in Fig. 11(a), the switching frequency freely runs to about 4 MHz. The ultra-high frequency is a big challenge for the design of the high-speed current sensor and the digital controller. Besides, under the light load, the high-frequency-related loss, such as the switching turn-OFF loss, magnetic core loss and high-frequency ac-current-related conduction loss, should severely reduce the efficiency.

Fig. 11(b) shows the switching frequency distribution with this proposed ZVS control method from full load to 5% of the full load. This figure shows the limited switching frequency range. The maximum frequency is accurately clamped to 1.5 MHz. Under full load condition, the maximum frequency is 0.95 MHz. When the load decreases to about half load, the frequency clamping starts to work. And during a short time under the half load condition, the frequency is clamped to 1.5 MHz. However, when the load decreases to even the lighter load, the frequency clamping works for a much longer time. Due to this frequency limitation, it is much easier for the design of the high-speed current sensor and the digital controller. In addition, under the light load, the frequency-related loss should be significantly reduced.

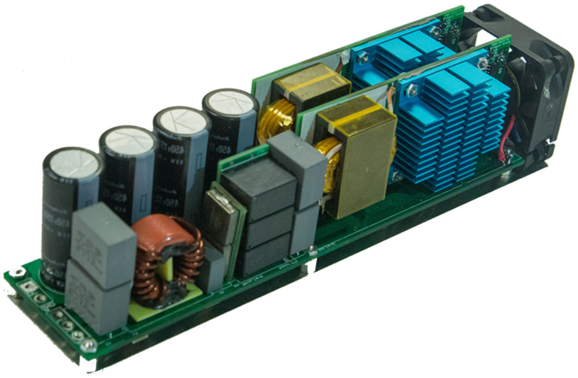

Fig. 12. Prototype of the proposed 3.2-kW GaN totem-pole PFC.

VI. HARDWARE IMPLEMENTATION AND EXPERIMENTAL VERIFICATION

To verify the proposed ZVS control method and system control strategy for the MHz GaN totem-pole PFC, a 3.2-kW GaN-based totem-pole PFC prototype with peak 99% efficiency is implemented in this paper, as shown in Fig. 12. There are two interleaved GaN totem-pole PFC phases in this prototype, and each phase is 1.6 kW. The size of this prototype is 7.9 in × 1.8 in × 1.8 in. The power density is about 130 W/in^3. Since the two-phase interleaving control is beyond the scope of this paper, only the testing for a single-phase 1.6-kW GaN totem-pole PFC is presented in this paper.

Both S_1 and S_2 use two 650-V driver-integrated eMode GaN devices (Navitas NV6117, 650 V, 120 mΩ) in parallel. In the Si leg, both S_3 and S_4 use two Si SJ MOSFETs IPL65R070C7 (650 V, 75 mΩ) in parallel. The inductor uses a Ferrite core ELP32 with Hitachi material ML91S. And for the winding, the inductor uses the litz-wire 46/920. And the inductance is 9.5 μH. The dc-link bulky capacitors are four E-caps (450BXW120-MEFR18X35) in parallel. The control system as shown in Fig. 8 is implemented in a single TI DSP TMS320F28075, which has a 120-MHz system clock. The maximum switching frequency limitation $f_{s\_\max}$ is 1.5 MHz and the required minimum ZVS time margin $T_{\mathrm{ZVS\_min}}$ is 30 ns. 1.5 MHz is close to the maximum switching frequency under the half load condition without frequency clamping. And choosing 1.5 MHz as the maximum switching frequency is a tradeoff between the conduction loss and the frequency-related loss. The reason to choose 30 ns as the minimum ZVS time margin is that the distribution of the total delay of the isolator, the driver (integrated with the GaN FET) and the sensor is about 30 ns. The parameters for experiments are the same with the previous parameters, and they are summarized again as follows: $V_{in} = 240$ VAC, $V_{out} = 400$ V,

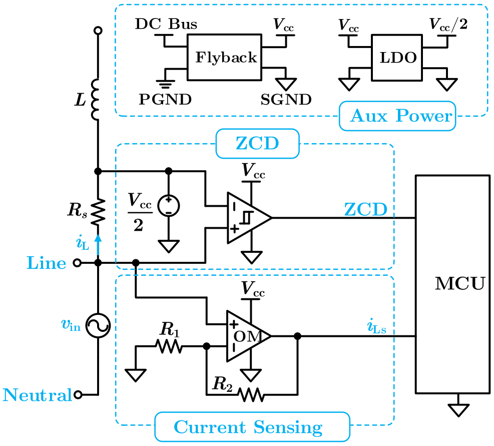

Fig. 13. Current sensing and ZCD circuits.

$P_{out} = 1.6$ kW, $L = 9.5$ μH, $C_{oss} = 120$ pF, $T_{ZVS\_min} = 30$ ns, and $f_{s\_max} = 1.5$ MHz.

The high-speed current sensing is another challenge in this high-frequency converter. To avoid the isolated high-speed current sensing, this paper proposes to put the control signal ground to the ac side. As shown in Fig. 13, one terminal of the sensing resistor is connected to the line point of the ac voltage. And, the half of the control power supply V_{cc} is connected to the other terminal of the sensing resistor. Then, the sensed voltage of R_s is level shifted to a positive voltage. The ZCD signal is the output of a high-speed comparator. And the ZCD signal can be directly connected to the micro-controller unit (MCU). The sensed inductor current signal is processed by a high-speed operational amplifier (OPAMP), and then transferred to the MCU for instantaneous comparison. Since there is no isolation for the current sensing with the proposed sensing solution, there is no digital isolator for transferring the ZCD signal, and the current sensing circuit is also very simple. The shunt resistor used is LVK25R005FER (5 mΩ, four terminals, and wide 2512 package). The OPAMP used is OPA838IDBVR. The comparator used is LMV7219. In Fig. 13, the auxiliary power is provided from the output dc link through an isolated converter. PGND is the power ground, which is the negative terminal of the dc link. SGND is the control circuit ground.

As discussed previously, with the conventional TCM ZVS control [22], [29], partial ZVS may occur, since there is no ZVS time margin when the input voltage is higher than half of the output voltage. Fig. 14 shows the partial ZVS switching waveforms with the conventional TCM ZVS control. The testing conditions of Fig. 14 are as follows: $V_{in} = 300$ V, $V_{out} = 400$ V, $I_{in} = 1.5$ A, and $f_s = 1.1$ MHz. As shown in Fig. 14(a), the SR turn-OFF current is only sufficient to make the drain-to-source voltage v_{ds2} of S_2 resonant to zero at one instant. Therefore, when S_2 is turned-ON 30 ns after the ZVS instant, v_{ds2} will be resonant back to 60 V as shown in Fig. 14(a). Thus, S_2 is turned ON with partial ZVS. As shown in Fig. 14(b), when S_2 is turned ON 30 ns before the ZVS instant, S_2 is also turned ON with partial ZVS. In Fig. 14(a) and (b), although S_2 is turned ON under the voltages that are much less than the output dc voltage, the switching loss is still considerable especially under MHz switching frequency and light-load conditions.

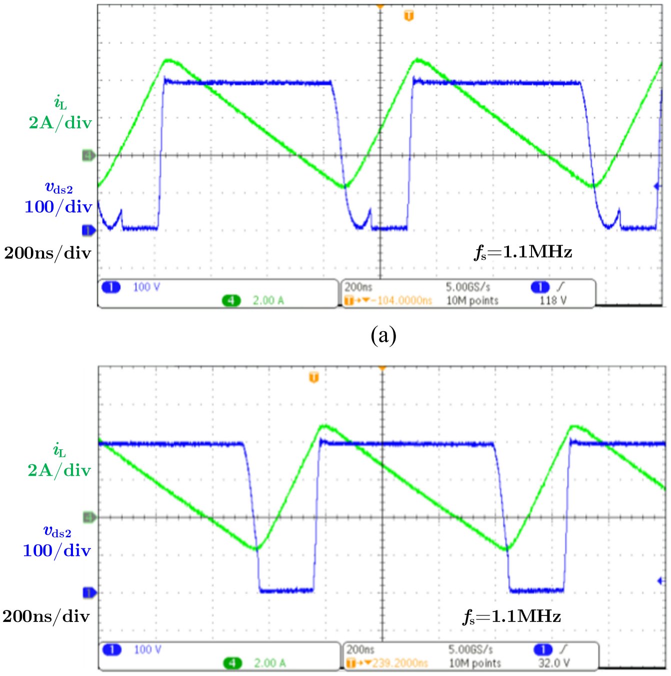

(a)

(b)

Fig. 14. Partial ZVS switching waveforms with the conventional TCM ZVS control, when there is no ZVS time margin under the following conditions $V_{in} = 300$ V, $V_{out} = 400$ V, $I_{in} = 1.5$ A. (a) Turn ON S_2 after the available ZVS instant. (b) Turn ON S_2 before the available ZVS instant.

However, with the proposed ZVS control, ZVS operation can be achieved at any instant during the improved ZVS time margin T_{zvs} as discussed previously. Fig. 15 shows the ZVS switching waveforms with improved ZVS time margin based on the proposed ZVS control. The testing conditions of Fig. 15 are as follows: $V_{in} = 300$ V, $V_{out} = 400$ V, $I_{in} = 1.5$ A, and $f_s = 1.0$ MHz. Fig. 15(a) shows the ZVS waveforms within several switching cycles. And Fig. 15(b) is the zoomed-in picture of Fig. 15(a). Compared with the conventional TCM ZVS control, the proposed ZVS control introduces more negative SR turn-OFF current. Then, the ZVS time margin is improved, and the switching frequency is also reduced.

Fig. 16 shows the ZVS operation waveforms for the developed GaN totem-pole PFC with the proposed ZVS control during the positive half-line cycle. The full-load testing waveforms are shown in Fig. 16(a) and (b), and the full-load testing conditions are as follows: $P_{out} = 1.6$ kW and $V_{out} = 400$ V. In Fig. 16(a), $V_{in} = 340$ V, and in Fig. 16(b), $V_{in} = 130$ V. As shown in Fig. 16(a) and (b), whenever V_{in} is less or more than 0.5 V_{out}, ZVS can always be realized with the proposed ZVS control. The switching frequency in Fig. 16(a) is 270 kHz, and the switching frequency in Fig. 16(b) is 920 kHz. Both the switching frequencies in Fig. 16(a) and (b) are conformed with the calculations based on the proposed ZVS control. The light-load testing waveforms are shown in Fig. 16(c), and the light-load testing conditions are as follows: $P_{out} = 0.32$ kW and $V_{out} = 400$ V. Fig. 16(c) shows that, at light load, ZVS can be achieved and the switching frequency is limited to 1.5 MHz with the proposed ZVS control. Therefore, the proposed ZVS control, which predictively controls the SR turn-OFF current to the

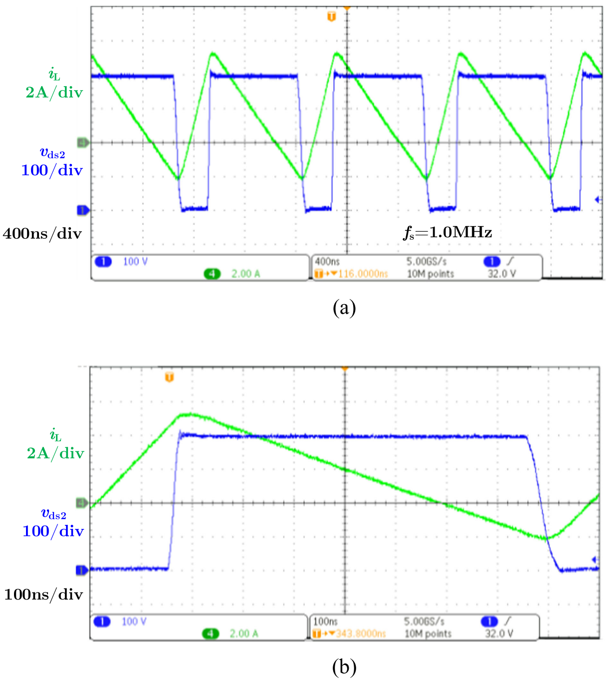

(a)

(b)

Fig. 15. ZVS switching waveforms with improved ZVS time margin based on the proposed ZVS control, under the following conditions $V_{\rm in}$ = 300 V, $V_{\rm out}$ = 400 V, and $I_{\rm in}$ = 1.5 A. (a) ZVS switching waveforms with several switching cycles. (b) zoomed-in ZVS switching waveforms.

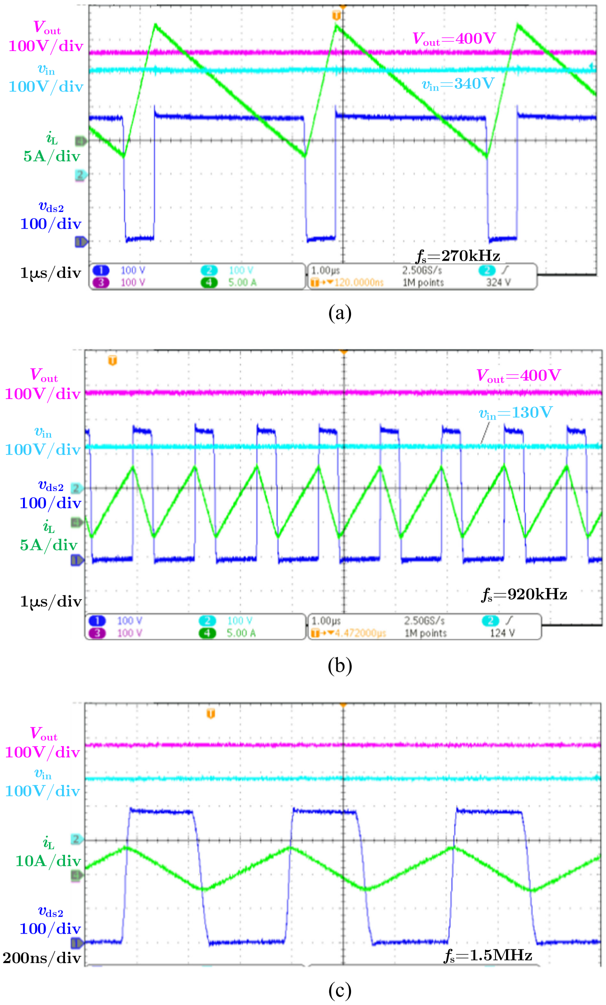

(a)

(b)

(c)

Fig. 16. ZVS operation waveforms with the proposed ZVS control during the positive half-line cycle. (a) $P_{\rm out}$ = 1.6 kW, $V_{\rm out}$ = 400 V, $V_{\rm in}$ = 340 V, and f_s = 270 kHz. (b) $P_{\rm out}$ = 1.6 kW, $V_{\rm out}$ = 400 V, $V_{\rm in}$ = 130 V, and f_s = 920 kHz. (c) $P_{\rm out}$ = 320 W, $V_{\rm out}$ = 400 V, $V_{\rm in}$ = 180 V, and f_s = 1.5 MHz.

required value as (20), not only gives enough margin to guarantee ZVS, but also limits the maximum frequency to the required value.

Fig. 17 shows the comparison of the measured switching frequency distribution and the calculated switching frequency distribution. The measured frequency distribution accurately matches the calculated switching frequency, with the proposed predictive ZVS control.

Fig. 18 demonstrates full-load operation waveforms during several line cycles. Fig. 18 shows that, with the proposed ZVS control and hybrid current control, the peak and valley currents of the inductor are well controlled. Besides, the ac input current is also controlled to be sinusoidal ac wave shape.

Fig. 19 shows the start-up waveforms of the totem-pole PFC with the proposed ZVS and system control. Before start-up, the output voltage is charged to the peak value of the ac voltage through a bridge diode. Then, the totem-pole PFC is softly started with zero load. Even during the zero-load soft start, the peak and valley currents of the inductor are still well controlled for ZVS operation and ac current regulation. When the output voltage reaches around 400 V, the load is connected, and the full-load operation is started. Thus, the soft start-up performance of the totem-pole PFC with the proposed control is shown in Fig. 19.

Fig. 20 shows the efficiency curve of this developed GaN totem-pole PFC from 10% to 100% of full load. The efficiency is measured by the power analyzer YOKOGAWA WT3000E. From half load to full load, the efficiency exceeds 99% and the curve is flat during this load range. With the decrease of the load, the efficiency also decreases. However, the efficiency is still around 98%. Even at 10% of full load, the efficiency is also kept around 97%. This great performance of efficiency is contributed by the proposed ZVS control. As shown in Fig. 9(a), at heavy load, this totem-pole PFC works with ZVS requirement and minimum ZVS time margin requirement, therefore, the heavy-load efficiency benefits by the ZVS operation and low circulating current. As shown in Fig. 9(b), at the light load, the switching frequency is clamped by the maximum switching frequency limitation requirement, therefore, the light-load efficiency benefits by the ZVS operation and the greatly reduced frequency related loss, such as the ac winding loss, core loss and switching turn-off loss. The proposed ZVS control achieves a good tradeoff between the conduction loss and the frequency-related loss. This measured efficiency does not include the loss of the dc fan and the micro-controller, since the dc fan and the micro-controller are shared by the whole two-phase 3.2-kW system. And the loss of the dc fan is 1.5 W. And the loss on the micro-controller is 2 W.

The loss breakdown under the full-load 1.6-kW condition has been analyzed in Fig. 21. Under the full-load condition, the maximum frequency is 0.95 MHz as shown in Fig. 17. There

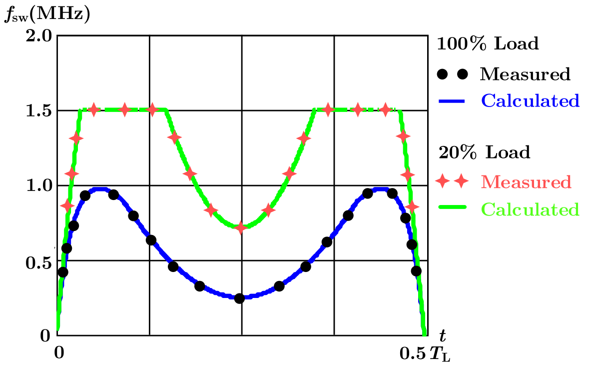

Fig. 17. Comparison of the tested switching frequency distribution and the calculated switching frequency distribution.

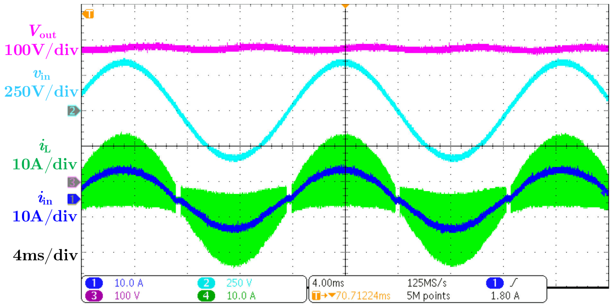

Fig. 18. Full-load operation waveforms during two line cycles with the proposed ZVS and system control.

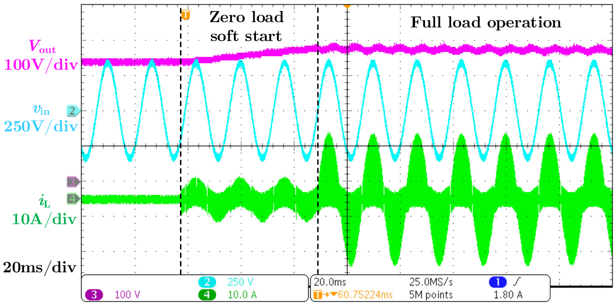

Fig. 19. Start-up waveforms with the proposed ZVS and system control.

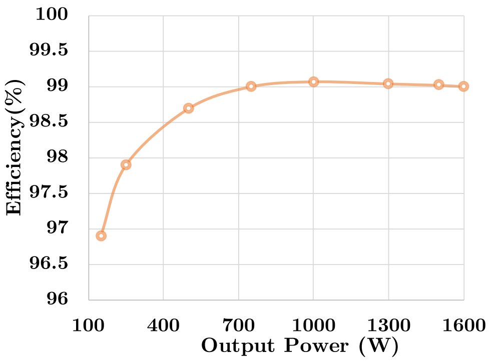

Fig. 20. Efficiency curve.

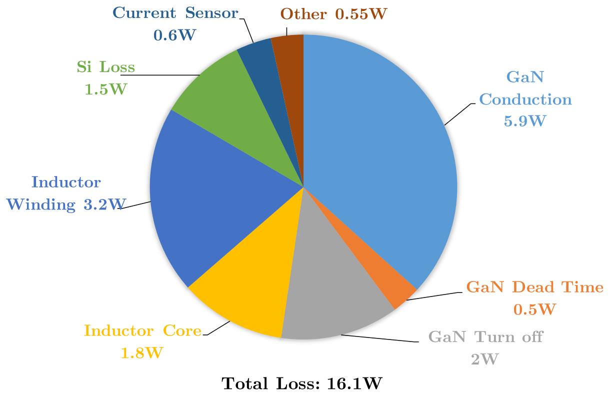

Fig. 21. Loss breakdown for the full-load 1600-W output power.

is no turn-ON loss due to the proposed full range ZVS control. The turn-OFF loss is only 2 W due to the utilization of GaN devices. As shown in Fig. 21, for the ZVS totem-pole PFC, the GaN conduction loss and the inductor loss dominate the total power loss. Therefore, using the GaN devices that have lower ON-resistances can further improve the efficiency.

VII. CONCLUSION

In this paper, a predictive ZVS control with improved ZVS time margin and limited switching frequency range for a 99% efficient MHz ZVS GaN totem-pole PFC rectifier is proposed and analyzed. First, this paper proposes that the SR turn-OFF current is a new degree of freedom for the ZVS control. And, by controlling the SR turn-OFF current, the ZVS time margin and the switching frequency can be accurately and continuously controlled. Thus, this paper proposes to control the SR turn-OFF currents to extend the ZVS time margin and reduce the maximum switching frequency. In this paper, the proposed predictive ZVS control method predictively controls the SR turn-OFF currents to be the required values that satisfy all the ZVS requirement, the minimum ZVS margin requirement and the maximum frequency limitation requirement. Then, the proposed predictive ZVS control achieves the minimum ZVS time margin and the maximum switching frequency limitation for the full range of the input and output voltages and the full range of the output power. The extended ZVS time margin improves the reliability for ZVS realization. The limited maximum frequency and the limited frequency range reduce the difficulty for the high-speed current sensing and the digital control, and also reduce the frequency-related loss especially under light-load conditions. In this proposed ZVS control, the SR turn-OFF current is predictively and accurately controlled by the extended SR conduction time T_{SR2}. Moreover, an analytical model of the ZVS totem-pole PFC is proposed to accurately extract all the current and timing parameters for the proposed ZVS control. The proposed ZVS control and analytical model are applicable for the full range of the input and output voltages, and for the fullrange of the load. Based on the proposed ZVS control, a hybrid current control is also proposed. In this current control, the peak current comparison generates the active switch turn-OFF instant. And, the required extended SR conduction time generates the SR turn-OFF instant. Therefore, this hybrid current control combines the benefits of the current mode control and the time-based control. Finally, a 3.2-kW MHz GaN totem-pole PFC prototype is developed and tested with the full range ZVS, minimum ZVS time margin, limited switching frequency range, 99% peak efficiency, and 130-W/in^3 power density based on the proposed ZVS control and system control strategy. With the proposed ZVS control method, the system efficiency exceeds 99% from the half load to full load. For the light load, with the frequency clamping, the efficiency is still around 98%. Even at 10% of the full load, the efficiency is also kept about 97%.

ACKNOWLEDGMENT

The authors would like to thank Navitas Semiconductor for GaN device sample.

REFERENCES

[1] F. C. Lee, Q. Li, Z. Liu, Y. Yang, C. Fei, and M. Mu, "Application of GaN devices for 1 kW server power supply with integrated magnetics," *CPSS Trans. Power Electron. Appl.*, vol. 1, no. 1, pp. 3–12, Dec. 2016.

[2] Q. Huang and A. Q. Huang, "Review of GaN totem-pole bridgeless PFC," *CPSS Trans. Power Electron. Appl.*, vol. 2, no. 3, pp. 187–196, Sep. 2017.

[3] L. Zhou, Y. Wu, J. Honea, and Z. Wang, "High-Efficiency true bridgeless totem pole PFC based on GaN HEMT: Design challenges and cost-effective solution," in *Proc. Int. Exhib. Conf. Power Electron. Intell. Motion, Renewable Energy Energy Manage.*, Nuremberg, Germany, 2015, pp. 1–8.

[4] B. Singh, B. N. Singh, A. Chandra, K. Al-Haddad, A. Pandey, and D. P. Kothari, "A review of single-phase improved power quality AC-DC converters," *IEEE Trans. Ind. Electron.*, vol. 50, no. 5, pp. 962–981, Oct. 2003.

[5] J. Chen, A. Prodic, R. W. Erickson, and D. Maksimovic, "Predictive digital current programmed control," *IEEE Trans. Power Electron.*, vol. 18, no. 1, pp. 411–419, Jan 2003.

[6] C. Qiao and K. M. Smedley, "A topology survey of single-stage power factor corrector with a boost type input-current-shaper," *IEEE Trans. Power Electron.*, vol. 16, no. 3, pp. 360–368, May 2001.

[7] M. M. Jovanovic and Y. Jang, "State-of-the-art, single-phase, active power-factor-correction techniques for high-power applications—An overview," *IEEE Trans. Ind. Electron.*, vol. 52, no. 3, pp. 701–708, Jun. 2005.

[8] Y. Jang and M. M. Jovanovic, "A Bridgeless PFC boost rectifier with optimized magnetic utilization," *IEEE Trans. Power Electron.*, vol. 24, no. 1, pp. 85–93, Jan. 2009.

[9] L. Huber, Y. Jang, and M. M. Jovanovic, "Performance evaluation of bridgeless PFC boost rectifiers," *IEEE Trans. Power Electron.*, vol. 23, no. 3, pp. 1381–1390, May 2008.

[10] F. Musavi, W. Eberle, and W. G. Dunford, "A High-Performance Single-Phase bridgeless interleaved PFC converter for plug-in hybrid electric vehicle battery chargers," *IEEE Trans. Ind. Appl.*, vol. 47, no. 4, pp. 1833–1843, Jul./Aug. 2011.

[11] F. Musavi, M. Edington, W. Eberle, and W. G. Dunford, "Evaluation and efficiency comparison of front end AC-DC plug-in hybrid charger topologies," *IEEE Trans. Smart Grid*, vol. 3, no. 1, pp. 413–421, Mar. 2012.

[12] B. Su and Z. Lu, "An interleaved Totem-Pole boost bridgeless rectifier with reduced reverse-recovery problems for power factor correction," *IEEE Trans. Power Electron.*, vol. 25, no. 6, pp. 1406–1415, Jun. 2010.

[13] W. Wu, "1.5 kW digital totem pole PFC design for Air-Conditioner and performance comparison using IGBT, SiC and GaN," in *Proc. Int. Exhib. Conf. Power Electron. Intell. Motion, Renewable Energy Energy Manage.*, Nuremberg, Germany, 2017, pp. 1–5.

[14] L. Xue, Z. Shen, D. Boroyevich, and P. Mattavelli, "GaN-based high frequency totem-pole bridgeless PFC design with digital implementation," in *Proc. IEEE Appl. Power Electron. Conf. Expo.*, Mar. 2015, pp. 759–766.

[15] Q. Huang, R. Yu, A. Q. Huang, and W. Yu, "Adaptive zero-voltage-switching control and hybrid current control for high efficiency GaN MHz Totem-pole PFC rectifier," in *Proc. IEEE Appl. Power Electron. Conf. Expo.*, Tampa, FL, USA, 2017, pp. 1763–1770.

[16] GaN Systems, High Efficiency CCM Bridgeless Totem Pole PFC Design using GaN E-HEMT, 2017. [Online]. Available: http://gansystems.com/wp-content/uploads/2018/01/GS665BTP-REF-rev170905.pdf

[17] A. Q. Huang, "Wide bandgap (WBG) power devices and their impacts on power delivery systems," in *Proc. IEEE Int. Electron Devices Meeting*, San Francisco, CA, USA, 2016, pp. 20.1-1–20.1-4.

[18] E. A. Jones, F. F. Wang, and D. Costinett, "Review of commercial GaN power devices and GaN converter design challenges," *IEEE J. Emerg. Sel. Topics Power Electron.*, vol. 4, no. 3, pp. 707–719, Sep. 2016.

[19] E. Persson, "How 600 V GaN transistors improve power supply efficiency and density," *Power Electron. Europe*, no. 2, pp. 21–24, Mar. 2015.

[20] E. Persson, "Practical application of 600 V GaN HEMTs in power electronics," in *Proc. IEEE Appl. Power Electron. Conf. Expo.*, Mar. 2015, pp. 3751–3758.

[21] Y. Yang, Z. Liu, F. C. Lee, and Q. Li, "Analysis and filter design of differential mode EMI noise for GaN-based interleaved MHz critical mode PFC converter," in *Proc. IEEE Energy Convers. Congress Expo.*, Pittsburgh, PA, USA, 2014, pp. 4784–4789.

[22] Z. Liu, F. C. Lee, Q. Li, and Y. Yang, "Design of GaN-Based MHz Totem-Pole PFC rectifier," *IEEE J. Emerg. Sel. Topics Power Electron.*, vol. 4, no. 3, pp. 799–807, Sep. 2016.

[23] Z. Liu, Z. Huang, F. C. Lee, and Q. Li, "Digital-based interleaving control for GaN-based MHz CRM Totem-pole PFC," in *Proc. IEEE J. Emerging Sel. Topics Power Electron.*, vol. 4, no. 3, pp. 808–814, Sep. 2016.

[24] Z. Liu, X. Huang, M. Mu, Y. Yang, F. C. Lee, and Q. Li, "Design and evaluation of GaN-based dual-phase interleaved MHz critical mode PFC converter," in *Proc. IEEE Energy Convers. Congress Expo.*, Pittsburgh, PA, USA, 2014, pp. 611–616.

[25] J. W. Kim, H. S. Youn, and G. W. Moon, "A digitally controlled critical mode boost power factor corrector with optimized additional on time and reduced circulating losses," *IEEE Trans. Power Electron.*, vol. 30, no. 6, pp. 3447–3456, Jun. 2015.

[26] Y. S. Lai, C. A. Yeh, and K. M. Ho, "A family of predictive digital-controlled PFC under boundary current mode control," *IEEE Trans. Ind. Informat.*, vol. 8, no. 3, pp. 448–458, Aug. 2012.

[27] C. Marxgut, J. Biela, and J. W. Kolar, "Interleaved triangular current mode (TCM) resonant transition, single phase PFC rectifier with high efficiency and high power density," in *Proc. Int. Power Electron. Conf.*, Sapporo, Japan, 2010, pp. 1725–1732.

[28] B. Su, J. Zhang, and Z. Lu, "Totem-Pole boost bridgeless PFC rectifier with simple Zero-Current detection and Full-Range ZVS operating at the boundary of DCM/CCM," *IEEE Trans. Power Electron.*, vol. 26, no. 2, pp. 427–435, Feb. 2011.

[29] C. Marxgut, F. Krismer, D. Bortis, and J. W. Kolar, "Ultraflat interleaved triangular current mode (TCM) single-phase PFC rectifier," *IEEE Trans. Power Electron.*, vol. 29, no. 2, pp. 873–882, Feb. 2014.

[30] J. Biela, D. Hassler, J. Miniböck, and J. W. Kolar, "Optimal design of a 5 kW/dm3/98.3% efficient TCM resonant transition single-phase PFC rectifier," in *Proc. Int. Power Electron. Conf.*, Sapporo, Japan, 2010, pp. 1709–1716.

[31] L. Huber, B. T. Irving, and M. M. Jovanovic, "Effect of valley switching and Switching-Frequency limitation on Line-Current distortions of DCM/CCM boundary boost PFC converters," *IEEE Trans. Power Electron.*, vol. 24, no. 2, pp. 339–347, Feb. 2009.

[32] Onsemi, NCP1616 Datasheet, 2017. [Online]. Available: http://www.onsemi.com/pub/Collateral/NCP1616-D.PDF

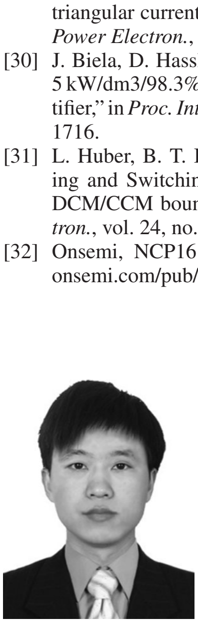

Qingyun Huang (S'14–M'18) received the B.Sc. degree in electrical engineering from Southwest Jiaotong University, Chengdu, China, in 2010, the M.Sc. degree in electrical engineering from Xi'an Jiaotong University, Xi'an, China, in 2013, and the Ph.D. degree in electrical engineering from the University of Texas at Austin, Austin, TX, USA, in 2018.

He is currently a Postdoctoral Research Fellow with the Department of Electrical and Computer Engineering, University of Texas at Austin. His current research interests include wide bandgap devices' applications, isolated/nonisolated dc–dc converters, grid-tied inverters, bridgeless PFC rectifiers, multilevel converters, soft-switching power converters, and digital control applied to power electronics and system modeling of power converters.

Ruiyang Yu received the B.E. degree in electrical engineering from Shandong University, Jinan, China, in 2007, and the M.S. and Ph.D. degrees in power electronics from The University of Hong Kong, Hong Kong, in 2008 and 2013, respectively.

He was a Postdoctoral Research Fellow from 2013 to 2017 and an Instructor in 2016 with North Carolina State University. He is currently a Research Associate with The University of Texas at Austin, Austin, TX, USA. His research interests include high-frequency and high power density power converter designs, magnetic component designs, and power converter control.

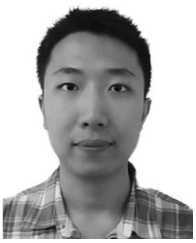

Qingxuan Ma (S'16) received the B.S. degree in electrical engineering from the Hebei University of Technology, Tianjin, China, in 2014, and the M.S. degree in electrical engineering from North Carolina State University, Raleigh, NC, USA, in 2017. He is currently working toward the Ph.D. degree with the University of Texas at Austin, Austin, TX, USA.

His current research interests include high-frequency power conversion, wide bandgap power semiconductor devices applications, and digital control.

Alex Q. Huang (S'91–M'94–SM'96–F'05) was born in Zunyi, China. He received the B.Sc. degree in electrical engineering from Zheijiang University, Hangzhou, China, in 1983, the M.Sc. degree in electrical engineering from the Chengdu Institute of Radio Engineering, Chengdu, China, in 1986, and the Ph.D. degree from Cambridge University, Cambridge, U.K., in 1992.

From 1992 to 1994, he was a Research Fellow with Magdalene College, Cambridge. From 1994 to 2004, he was a Professor with the Bradley Department of Electrical and Computer Engineering, Virginia Polytechnic Institute and State University, Blacksburg, VA, USA. From 2004 to 2017, he was the Progress Energy Distinguished Professor of electrical and computer engineering with North Carolina State University, Raleigh, NC, USA, where he established and led the NSF FREEDM Systems Center. Since 2017, he has been the Dula D. Cockrell Centennial Chair in Engineering with the University of Texas at Austin, Austin, TX, USA. Since 1983, he has been involved in the development of modern power semiconductor devices and power integrated circuits. He fabricated the first IGBT power device in China in 1985. He is the inventor and a key developer of the emitter turn-OFF thyristor. He developed the concept of energy Internet and the smart-transformer-based energy router technology. His current research interests include power electronics, power management microsystems, and power semiconductor devices. He has mentored and graduated more than 80 Ph.D. and master students, and has authored and coauthored more than 500 papers in international conferences and journals. He has also been granted more than 20 U.S. patents.

Prof. Huang was the recipient of the NSF CAREER Award, the prestigious R & D 100 Award, and the MIT Technology Review's 2011 Technology of the Year Award.